


Research

Aspen Plus simulation of Chemical Looping Combustion of syngas and methane in fluidized beds

 Micah Jasper¹  · Abolghasem Shahbazi¹  · Keith Schimmel²  · Fanxing Li³  · Lijun Wang¹ 

Received: 31 October 2022 / Accepted: 17 January 2023

Published online: 04 February 2023

© The Author(s) 2023 

Abstract

Chemical Looping Combustion (CLC) is a technology that efficiently combines power generation and CO₂ capture. In CLC, the fuel is oxidized by a metal oxide called an oxygen carrier (OC). CLC uses two reactors: a fuel reactor and an air reactor. The fuel reactor oxidizes the fuel and reduces the OC. The air reactor oxidizes the OC using air and then the OC is cycled back to the fuel reactor. It is typical for both the fuel and the air reactors to be fluidized beds (FBs). In this research, an Aspen Plus model was developed to simulate a CLC system. Aspen Plus has recently included a built-in FB unit operation module. To our knowledge, no literature has been reported using this FB module for simulating fluidized bed combustion or gasification. This FB unit process was investigated in Aspen Plus and a kinetic based model was used and compared the simulation results to experimental data and the commonly used Gibbs equilibrium model. The FB unit and the kinetic model well fit the experimental data for syngas and methane combustion within 2% of the molar composition of syngas combustion and within 4% for the methane combustion. An advantage of this model over other kinetic models in literature is that the core shrinking model kinetic rate equations have been converted into a power law form. This allows Aspen Plus to use a calculator instead of an external Fortran compiler. This greatly simplifies the modeling process. The reaction rate equations are given for all reactions. A sensitivity analysis of the reaction kinetics was conducted. All data, code, and simulation files are given.

Keywords SCLC · Syngas · Methane · CLC · Chemical Looping · Combustion · Aspen Plus · Process simulation model

List of Symbols

A/n [m ²]	Distributor area per number of orifices [44] $A_T/n_d = 0.5 \text{ cm}^2$
A_{AR} [m ²]	Air reactor cross sectional area
A_{FR} [m ²]	Fuel reactor cross sectional area
AFR	Mass air–fuel ratio (MAFR)
AFR_{st}	Stoichiometric mass air–fuel ratio ($MAFR_{st}$)
CO/H ₂	Carbon-to-hydrogen ratio
D_{AR} [m]	Air reactor inner diameter
D_{FR} [m]	Fuel reactor inner diameter
d_o [m]	Diameter of orifices

Supplementary Information The online version contains supplementary material available at <https://doi.org/10.1007/s43938-023-00020-x>.

✉ Micah Jasper, m.jasper@aggies.ncat.edu; Abolghasem Shahbazi, ash@ncat.edu; Keith Schimmel, kaschimmel@olivet.edu; Fanxing Li, fli5@ncsu.edu; Lijun Wang, lwang@ncat.edu | ¹North Carolina Agricultural and Technical State University, Greensboro, NC, USA. ²Olivet Nazarene University, Bourbonnais, IL, USA. ³North Carolina State University, Raleigh, NC, USA.



$d_{p,D50}$ [m]	Solid particle diameter D_{50}
$D_{p,std}$ [m]	Solid particle standard deviation
D_R [m]	Riser diameter
F_{Fuel} [mol/h]	Inlet molar flowrate of fuel in FR
F_{MeO} [mol/h]	Molar flowrate of metal oxide
F_s [kg/h]	Solid mass flowrate (3–14 kg/h)
H_{AR} [m]	Air reactor height
H_{FR} [m]	Fuel reactor height
H_R [m]	Riser height
L_{AR} [m]	Air reactor bed height
L_{FR} [m]	Fuel reactor bed height
L_N [L]	Liter of gas at NTP 0 °C and 1 atm
M_{Ni} [kg/kmol]	Ni molar mass
M_{NiO} [kg/kmol]	NiO molar mass
m_{NiO} [kg/h]	NiO mass flowrate
NAFR	Molar air–fuel ratio (NAFR)
NAFR _{st}	Stoichiometric molar air–fuel ratio (NAFR _{st})
N_{Air} [mol/h]	Molar flowrate of air
n_{AR}	Number of orifices in distributor
N_{CO} [mol/h]	Molar flowrate of CO
N_{CO2} [mol/h]	Molar flowrate of CO ₂
n_{FR}	Number of orifices in distributor
N_{Fuel} [mol/h]	Molar flowrate of fuel
N_{H2} [mol/h]	Molar flowrate of H ₂
N_{H2O} [mol/h]	Molar flowrate of H ₂ O
N_{LS} [mol/h]	Molar flowrate of loop seal
N_{N2} [mol/h]	Molar flowrate of N ₂
N_{NiO} [kmol/h]	NiO molar flowrate
N_{NiO} [mol/h]	NiO molar flowrate
%NiO	NiO mass fraction of particle
P [atm]	Normal pressure
Q_{AR} [L _N /h]	Gas flow in the air reactor
Q_{FR} [L _N /h]	Gas flow in the fuel reactor
Q_{LS} [L _N /h]	Gas flow in the loop seal
R [m ³ ·atm/(K·kmol) mJ/kmol/K]	Universal gas constant
T [°C]	Normal temperature
T_{AR} [K]	Average temperature in air reactor
T_{FR} [K]	Average temperature in fuel reactor
$V_{b,AR}$ [m ³]	Volume of bed in fuel reactor
$V_{b,FR}$ [m ³]	Volume of bed in fuel reactor
$V_m = V/n = M/\rho$ [L/mol]	Molar volume
%V _{CH4} [%vol]	Volumetric percent of CH ₄
%V _{CO} [%vol]	Volumetric percent of CO
%V _{CO2} [%Vol]	Volumetric percent of CO ₂
%V _{H2} [%vol]	Volumetric percent of H ₂
%V _{H2O} [%vol]	Volumetric percent of H ₂ O
%V _{N2} [%vol]	Volumetric percent of N ₂
W_{AR} [kg]	Fuel reactor solid loading
W_{FR} [kg]	Fuel reactor solid loading
λ	Air–fuel equivalence ratio
ρ_b [kg/m ³]	Bulk density of solid OC
$\rho_{b,AR}$ [kg/m ³]	Bulk density of solid OC
$\rho_N = n/V$ [kmol/m ³]	Molar density

φ	Mass oxygen carrier-to-fuel ratio (MOCFR)
Φ	Oxygen carrier-to-fuel equivalence ratio (OCFER)
φ_N	Molar oxygen carrier-to-fuel ratio (NOCFR) $\varphi_N = F_{MeO}/F_{Fuel}$
$\varphi_{N,st}$	Stoichiometric molar oxygen carrier-to-fuel ratio (NOCFR _{st})
φ_{st}	Stoichiometric mass oxygen carrier-to-fuel ratio (MOCFR _{st})

Abbreviations

CLC	Chemical looping combustion
CLG	Chemical looping gasification
OC	Oxygen carrier
FB	Fluidized bed
GHG	Greenhouse gas
MEA	Monoethanolamine (used in CO ₂ scrubbing)
CSTR	Continuously stirred tank reactor
PFR	Plug flow reactor
CLBG	Chemical looping biomass gasification
CLG	Chemical looping gasification
BET	Brunauer, Emmett and Teller theory used to get specific surface area (m ² /g)
FR	Fuel reactor
AR	Air reactor
LS	Loop seal
BB	Bubbling bed
ER	Equivalence ratio
AFER	Air–fuel equivalence ratio λ
AFR	Air–fuel ratio
NOR	N ₂ /O ₂ ratio
OCFER	Oxygen carrier-to-fuel equivalence ratio
OCFR	Oxygen carrier-to-fuel ratio
SCM	Shrinking core model
Me	Transition metal used as the oxygen carrier
NTP	Normal temperature and pressure (0 °C and 1 atm)
PSD	Particle size distribution
ST	Stoichiometric
MNC	Methane Nickel-oxide Combustion
HNC	Hydrogen Nickel-oxide Combustion
CNC	CO Nickel-oxide Combustion
NO	Nickel Oxidation
MNPOX	Methane Nickel-oxide Partial Oxidation
WGS	Water Gas Shift Reaction
RWGS	Reverse Water Gas Shift Reaction
SMR	Steam Methane Reforming
RSMR	Reverse Steam Methane Reforming
MCO	Methanation with Carbon Monoxide = RSMR
MCO ₂	Methanation with Carbon Dioxide
DMR	Dry Methane Reforming
RDMR	Reverse Dry Methane Reforming
MD	Methane Decomposition
RMD	Reverse Methane Decomposition
CM	Char Methanation = RMD
SG	Steam Gasification Reaction = Water–Gas Reaction
WG	Water–Gas Reaction = Steam Gasification Reaction
CG	CO ₂ Gasification = Reverse Boudouard Reaction
RCG	Reverse CO ₂ Gasification

BR
RBRBoudouard Reaction
Reverse Boudouard Reaction = CO₂ Gasification

1 Introduction

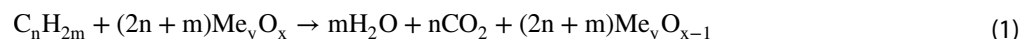
The world has an ever-increasing need for clean energy to help reduce global warming driven by human generated greenhouse gas (GHG) emissions. Carbon dioxide (CO₂) accounts for about 80% of anthropogenic GHG emissions and methane accounts for approximately 10% [1, 2]. Further, more than 40% of all anthropogenic CO₂ emissions is produced by coal fired power plants [3].

Three main categories of carbon capture systems are: post-combustion capture, pre-combustion capture, and oxy-fuel combustion (also called oxy-combustion). Post-combustion capture removes the CO₂ from combustion flue gases after combustion using air, but these separation units often involve a large parasitic energy expense for fossil fuel power plants [4]. The most common method of post-combustion CO₂ separation uses monoethanolamine (MEA) scrubbing. The flue gas is cooled and enters an absorber where amine is used as a solvent to remove CO₂ from the flue gas stream. The amine solvent is then regenerated in a stripper unit where the temperature is higher than the absorber unit. CO₂ can then be recovered at lower pressure. MEA and other solvent scrubbers have many drawbacks, such as corrosion and energy intensive solvent regeneration [5–7]. Also the presence of other flue gas contaminants such as SO_x and NO_x negatively impact the solvent based scrubbers' performance. There are also CO₂ scrubbers specific to syngas. Materials such as zeolites, alumina molecular sieves, and activated carbon are used to adsorb CO₂ in the production of hydrogen from syngas and in natural gas "sweetening." But again, the regeneration of the adsorbent is often energy intensive [4]. Membranes can also be used to separate gases of different sizes, however, this has been difficult to scale and has high capital cost [7].

Chemical Looping Combustion (CLC) would be considered an oxy-combustion carbon capture technology in the previous three categories. It involves an intrinsic oxygen separation and is therefore a more efficient alternative for carbon capture [8–12]. CLC can operate with many different fuel types, including coal, biomass, and natural gas. Most exciting environmentally is that CLC and chemical looping gasification (CLG) can be carbon-negative [13, 14].

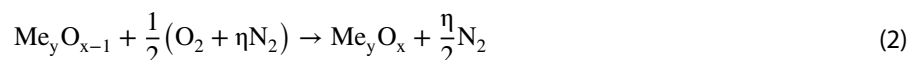
The CLC process usually uses a transition metal oxide as an oxygen carrier (OC) to transport oxygen from the air reactor (AR) to the fuel reactor (FR). The OC is circulated between the AR and the FR. The FR oxidizes the fuel and reduces the OC. The AR oxidizes the OC using air and then the OC is cycled back to the FR. This is illustrated in Fig. 1. In this way, the fuel does not need to be in contact with air, and the resulting combustion gases are free of nitrogen.

A generalized version of the reaction for a hydrocarbon fuel in the FR can be written:



where Me represents the transition metal in the oxygen carrier, Me_yO_x.

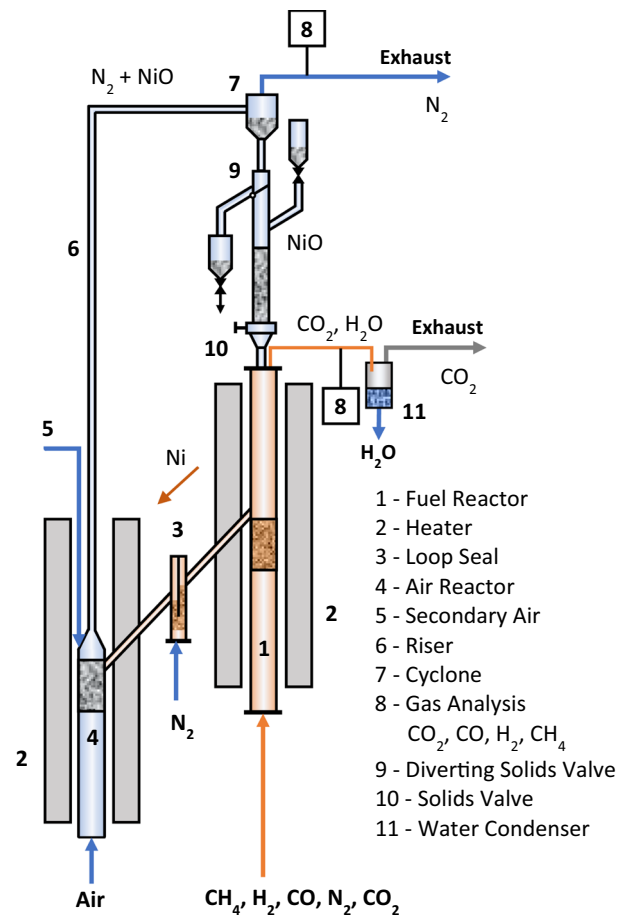
The reduced metal oxide Me_yO_{x-1} is then transported to the AR where it is re-oxidized in the following reaction:



where η is the N₂/O₂ ratio (NOR) usually assumed to be 3.76. Transition metals are particularly good oxygen carriers. Specifically, iron (Fe₂O₃/Fe₃O₄/FeO/Fe), copper (CuO/Cu), nitrogen (NiO/Ni), and manganese (Mn₂O₃/Mn₃O₄/MnO/Mn) are often used and studied [15–17]. The metal can be supported by an inert support, such as alumina (Al₂O₃), titania (TiO₂), silica (SiO₂), zirconia (ZrO₂), or bentonite, to increase the OC's durability, reactivity, and fluidizing properties [18]. Mixed metal oxides have also been studied recently and show promise. Ideal OC particles will have high oxygen carrying capacity, high oxidation and reduction reaction rates, high durability, appropriate particle size, density, and pore structure to allow high fluidization and reactivity.

Because the air, specifically the nitrogen, does not need to contact the fuel, CLC can avoid producing NO_x emissions [19]. When a simple hydrocarbon is completely combusted, like methane, it can produce a clean stream of CO₂ and H₂O. The water is easily condensed out and this leaves a pure stream of CO₂ for capture and utilization or storage. The gas stream leaving the air reactor is simply spent air. It contains mostly nitrogen and unreacted oxygen and can be released into the atmosphere with minimal environmental impact.

Fig. 1 Schematic of a circulating fluidized bed system for continuous chemical looping combustion (CLC) plant [37, 38]



To recover the lost energy, the hot air leaving the AR could drive a turbine. The exhaust from the FR can also be used to drive a gas turbine and then boil water in a combined gas and steam cycle system for efficient electricity generation. The reduction reaction of the metal oxide OC with fuel is usually endothermic, and the oxidation reaction of the OC with air is usually exothermic [20]. The heat of reaction will depend on the fuel and oxygen carrier used. The heat loss can be reduced by recovering low grade heat [21, 22]. Depending on the metal oxide used as the OC, the thermal energy generated in the fuel reactor is usually larger than the energy required for direct combustion of the fuel [22, 23]. Utilizing the waste heat makes this CLC system highly efficient [24]. Finally, after condensing the water from the exhaust, the remaining CO_2 is highly pure and concentrated and can be easily captured and utilized.

Process simulators, like Aspen Plus, Aspen Hysys, PRO/MAX, and PRO/II, are used in industry to model chemical and power plants. They are able to simulate a wide range of steady-state and dynamic thermodynamic and chemical processes. Process simulations have simple building blocks called unit processes which are usually continuously stirred tank reactors (CSTRs) or plug flow reactors (PFRs). Many process simulators, like Aspen Plus, also have many built in unit processes that can simulate complicated processes, like non-ideal reactors, catalytic reactors, solids processing, absorbers, and distillation columns. Mass and energy streams link each of the unit processes together. The process simulator then performs mass and energy balances on each of the blocks and the system as a whole.

Fluidized beds (FBs) have complex hydrodynamics and kinetics that need to be accurately modelled. Process simulators have not traditionally had built-in unit processes for fluidized beds, but Aspen Plus within the last few recent versions, introduced a more complete solids processing library that included a built-in fluidized bed reactor. Prior to this built-in reactor, there were a few common ways to simulate the fluidized bed.

The most common and simplest way to simulate combustion and gasification in Aspen Plus is by using a Gibbs equilibrium reactor [22, 25]. This unit process works by minimizing the Gibbs free energy and assuming equilibrium. It does not require a volume to calculate this equilibrium, and thus cannot give accurate sizing and pricing information. Also the Gibbs equilibrium models overestimate the conversion of species because mass transfer and kinetic limitations are neglected.

The other way to model fluidized bed combustors and gasifiers is by assuming the reactor is a series of PFRs or CSTRs or a combination of both. These methods are discussed in the studies of Jafari et al. [24] and Cui et al. [26, 27].

Finally, a more complex but more accurate model for fluidized beds is the three-phase model. Kunii and Levenspiel describe the three-phase model for fluidized beds as a series of CSTRs and PFRs in parallel with mass and energy exchange between them [28]. The bubble phase in a fluidized bed reactor are modeled as an ideal PFR rising through the reactor. The emulsion phase, which is the mixture of gas and solids is modeled as an ideal CSTR. The cloud phase, which is the tail and solids area around the bubbles can be modeled separately. A two-phase model, on the other hand, does not separately model the cloud phase. All phases at each level exchange mass and energy. A version of the two-phase model has been described specifically for sequential process simulators, like Aspen Plus, by Jafari et al. [24].

The following describes some examples of the two-phase model found in the literature that have influenced this work. Sarvar-Amini et al. [29] modelled a fluidized bed membrane reactor. Sotudeh-Gharebaagh et al. [30] and Liu et al. [31] modelled a fluidized bed for coal combustion (as a series of PFRs). Hashemi Sohi et al. [32] modelled a fluidized bed for natural gas combustion with a membrane reactor. Porrazzo et al. [21] modeled fluidized beds for chemical looping combustion of natural gas using NiO, and Rafati et al. [33] modeled chemical looping biomass gasification (CLBG). Ohlemüller et al. developed a kinetic model for coal CLC with a 100 kW pilot plant [34] and a 1 MW pilot plant [35]. Another very detailed kinetic model for fluidized bed gasification was made by Puig-Gamero et al. [36].

To our knowledge, there are no published models of combustion or gasification using the built-in Aspen Plus Fluidized Bed (FB) Unit Process. The aim of this work is to demonstrate the built-in FB reactor in Aspen Plus for CLC. An advantage of this model over other kinetic models in literature is that all of the shrinking core model (SCM) kinetics have been transformed to power law rate kinetics with the use of a calculator. This means that no external Fortran is needed. Most Aspen Plus CLC models used the RGIBBS reactor, but if they happen to use a kinetic based model, then most require an external Fortran compiler and linking with MS Visual Studio. This model simplifies the process. The reaction rate equations are given for all reactions in Table 6. The simulation results are compared to experimental data [37, 38] and to the commonly used Gibbs equilibrium model. Further, many parameters are explored for improving the combustion efficiency. The optimal operating conditions found for the described CLC system are given. This paper was originally part of a dissertation [39].

2 CLC process description

2.1 System configuration

This study was to develop an Aspen Plus based model to simulate the CLC process shown in Fig. 1 that was reported in literature described by Dueso et al. [37] and Adanez et al. [38]. The CLC setup has two interconnected fluidized beds working in two different fluidization regimes. Specifically, the reduction of the OC in the fuel reactor is carried out in a bubbling bed fluidization reactor, while the OC is oxidized in the air reactor which is a fluidized bed operating in the fast fluidization regime [28]. The energy and exergy analyses were already conducted by Adanez et al. [38].

A nickel-based catalyst which was 18% Ni supported on alpha alumina (Ni18- α Al) was used as the OC [37, 38]. The literature has shown that α -Al₂O₃ is the best form of alumina support for promoting reactivity of the Ni in a OC [40]. The main characteristics of the OC are given in Table 1.

2.2 The fuel reactor (FR) and air reactor (AR)

The fuel reactor (FR) is considered to be a bubbling bed (BB). A fluidized bed is in the bubbling bed regime when the value of the superficial gas velocity $U_{0,FR}$ is higher than that of the minimum fluidization velocity U_{mf} and lower than the terminal velocity of the particles U_t [28]. A bubbling bed can be modeled using the two-phase theory with a separate bubble phase (having a low concentration of solids) and an emulsion phase (assumed to have perfect mixing of gas and solids) co-existing in the bed. The emulsion phase is assumed to be at minimum fluidization conditions where gas that is rising faster than the minimum fluidization velocity (i.e., $U_0 > U_{mf}$) is transferred to the bubble phase. This is what the built-in Fluidized Bed (FB) reactor unit process in Aspen Plus does.

Assumptions related to the fuel reactor are [41, 42]:

1. Gas in the emulsion phase is equal to the minimum fluidization velocity ($U_e = U_{mf}$)

Table 1 Properties of the oxygen carrier Ni18- α Al fresh and used for 100 h [37, 38]

Property	Symbol	Units	Fresh	Used
NiO content	w_{NiO}	wt%	18	18
Oxygen Transport Capacity	R_{OC}	–	0.0386	0.0386
Particle Size	d_p	mm	0.1–0.3	0.1–0.3
Porosity	ϵ	–	0.40 ± 0.01	0.42 ± 0.01
Particle Density	ρ_p	kg/m ³	4290 ± 20	4250 ± 20
Bulk Density	ρ_b	kg/m ³	2470 ± 10	2480 ± 10
Specific Surface Area (BET)	S_{BET}	m ² /g	7.0 ± 0.2	6.8 ± 0.2
Crushing Strength	F^*	N	4.1 ± 0.3	3.7 ± 0.2

Table 2 CLC system parameters

Parameter	Symbol	Units	Fuel reactor	Air reactor	Source
Temperature	T	°C	880	950	[37, 38]
Bed Height	L	m	0.1	0.1	[37, 38]
Reactor Height	H	m	0.4	0.16	[37, 38]
Reactor Inner Diameter	D	m	0.05	0.05	[37, 38]
Cross-Sectional Area	A	m ²	0.001963	0.001963	Calculated
Distributor Area Per Orifices	A/n_o	m ²	0.00005	0.00005	[28, 44]
Diameter of Orifice	d_o	m	0.003536	0.003536	Assumed
Number of Orifices in Distributor	n_o	–	40	40	Calculated
Volume of Bed	V_b	m ³	0.000196	0.000196	Calculated
Bulk Density of Solid OC	ρ_b	kg/m ³	2470	2375	[37, 38]
Solid Loading	W_{FR}	kg	0.3	0.5	[37, 38]
Riser Height	H_R	m		1	[37, 38]
Riser Inner Diameter	D_R	m		0.02	[37, 38]
Primary Gas Flow (Fuel Air)	Q	L _N /h	170	720	[37, 38]
Secondary Gas Flow (Loopseal N ₂ Air)	Q ₂	L _N /h	37.5	150	[37, 38]
Normal Temperature (Inlet Gas)	T	°C	0	0	NTP [38, 43]
Normal Pressure	P	atm	1	1	NTP [38, 43]
Molar Flowrate	N	mol/h	7.5846	32.1228	Calculated
Secondary Molar Flowrate	N ₂	mol/h	1.673	6.6923	Calculated

2. The bubbling bed reactor is isothermal.
3. The solid density is considered constant in the horizontal plane (no variation radially)
4. The bubble diameter is assumed to be constant in the two-phase model

The air reactor is in the fast fluidization regime, which means that the superficial gas velocity at the inlet $U_{0,AR}$ is greater than U_t [28]. This means that the solids will be elutriated and will be carried by the gas out of the top of the reactor. In fast fluidization, the gas and solids are assumed to be perfectly mixed when modeling. Also, the solid volume fraction or solid density is assumed to be constant radially [28]. However, there are different solid densities vertically. There are two zones along the height of the riser: the dense bottom phase and the lean top phase. The lean top phase can be further divided into a lower acceleration region, an upper acceleration region, and a completely fluidized region [28, 30, 31]. The built-in FB unit process handles the elutriation model.

Table 2 gives parameters for the FR and AR. The temperature and pressure are given in NTP which is defined as 1 atm and 0 °C as specified in [38, 43] (the definition of NTP and STP can vary per region).

2.3 Calculating the syngas oxygen carrier to fuel equivalence ratio (OCFER) Φ

The air–fuel ratio can be mass based or molar based. In this research, MOCFR refers to the mass air–fuel ratio, and NOCFR refers to the molar oxygen carrier-to-fuel ratio. Each ratio is given by the formula below:

$$\phi = MOCFR = \frac{\dot{m}_{OC}}{\dot{m}_{Fuel}} = \frac{N_{OC}}{N_{Fuel}} \frac{M_{OC}}{M_{Fuel}}, \quad \phi_{st} = MOCFR_{st} = \frac{\dot{m}_{OC,st}}{\dot{m}_{Fuel,st}} \quad (3)$$

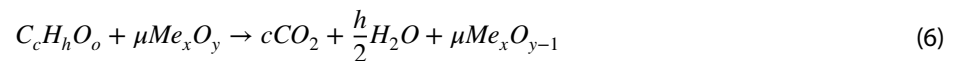
$$NOCFR = \frac{N_{OC}}{N_{Fuel}}, \quad NOCFR_{st} = \frac{N_{OC,st}}{N_{Fuel,st}} \quad (4)$$

$$\Phi = OCFER = \frac{\phi}{\phi_{st}} = \frac{MOCFR}{MOCFR_{st}} = \frac{\dot{m}_{OC}/\dot{m}_{Fuel}}{\dot{m}_{OC,st}/\dot{m}_{Fuel,st}} = \frac{NOCFR}{NOCFR_{st}} = \frac{N_{OC}/N_{Fuel}}{N_{OC,st}/N_{Fuel,st}} \quad (5)$$

where \dot{m}_{OC} the mass flowrate of oxygen carrier (OC) [kg/s], \dot{m}_{Fuel} the mass flowrate of fuel [kg/s], N_{OC} is the molar flowrate of OC [kmol/s], N_{Fuel} is the molar flowrate of fuel [kmol/s], M_{OC} is the molar mass of air [kg/kmol], and M_{Fuel} is the molar mass of fuel [kg/kmol].

A subscript of "st" denotes the stoichiometric NOCFR calculated from the reactions and equations below, to distinguish the $NOCFR_{st}$ from the actual NOCFR used in each simulation or experiment.

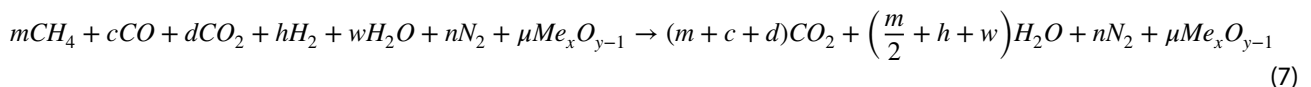
The general chemical looping stoichiometric combustion reaction for hydrocarbon fuels with oxygen is:



$$\mu = 2c + \frac{h}{2} - o = 2\alpha$$

where c denotes the moles of carbon, h the moles of hydrogen, o the moles of oxygen present in the fuel, μ is the moles of metal oxide OC needed for complete stoichiometric combustion the hydrocarbon fuel, α is the number of moles of O_2 needed for complete stoichiometric combustion of the hydrocarbon if air or pure O_2 where used.

The stoichiometric combustion of syngas can be represented as the following general reaction:



$$\mu = 4m + c + h = 2\alpha$$

$$f = N_{Fuel} = m + c + d + h + w + n, \quad \mu = N_{Me_x O_y, st} = N_{OC, st} = 4m + c + h$$

where m , c , d , h , w , and n are the molar flowrate of CH_4 , CO , CO_2 , H_2 , H_2O , and N_2 in syngas respectively (note the subscripts and coefficients are different than previously defined in Eq. 6), f is the total molar flowrate of syngas fuel, μ is the molar flowrate of the oxygen carrier $Me_x O_y$ for the stoichiometric combustion of syngas.

Below are the equations to calculate the molar based NOCFR and the equivalence ratio Φ .

$$NOCFR_{st} = \frac{N_{OC, st}}{N_{Fuel, st}} = \frac{\mu}{f} = \frac{4m + c + h}{m + c + d + h + w + n} \quad (8)$$

$$N_{Fuel} = N_{Fuel, st} = f \quad (\text{when not normalized}) \quad (9)$$

$$\Phi = OCFER = \frac{NOCFR}{NOCFR_{st}} = \frac{N_{OC}/N_{Fuel}}{N_{OC, st}/N_{Fuel, st}} = \frac{N_{OC}}{\mu} = \frac{N_{OC}}{4m + c + h} \quad (10)$$

2.4 Reduction and oxidation kinetics

In this research, two experiments are compared: one with syngas, the other with methane. A nickel oxygen carrier (NiO/Ni) supported by alumina $\alpha\text{-Al}_2\text{O}_3$ was used [37, 38]. The particles range from 0.1 to 0.3 mm The air flowing in the air

reactor is assumed to be 21% oxygen O₂ and the remaining percentage 79% is entirely nitrogen N₂ (argon, atmospheric CO₂ and H₂O, and all other minor constituents are neglected). Properties of the oxygen carrier are given in Table 1.

Oxidation and reduction kinetics have been studied for metal oxides and various gases including O₂, CO, CO₂, H₂, H₂O, and CH₄ [19, 45–47]. Other studies on CLC using methane and Ni based oxygen carriers [48–50] found similar reaction kinetics to Ryu et al. [45]. The SCM is often used to describe the core of unreacted metal oxide gradually reducing in size [18]. The SCM model provides a good fit with experimental data [15, 16, 18, 45, 50–52]. Furthermore, most reaction kinetics provided in literature for oxygen carriers are surface reaction rates with the pre-exponential factor of units m/s.

This simulation model makes the following assumptions [45, 53, 54]:

1. The particles are spherical.
2. The particles total volume remains constant, with only the ratio of unreacted core to the reacted shell changing.
3. The surface reaction is rate limiting, and the gas film diffusion and internal particle diffusion are fast compared to the surface reaction and can therefore be neglected.
4. The reaction and particle are isothermal.
5. The percent of deactivated NiO remains constant.
6. All NiAl₂O₄ is considered to be deactivated NiO since it has a much lower reactivity than NiO [55]

The study by Ryu et al. [45] determines that the reduction reaction rate for NiO/Ni particles supported by bentonite is controlled by the surface chemical reaction, while the oxidation rate is controlled by internal particle diffusion. Another two studies by Garcia-Labiano et al. [16, 50] showed how the chemical kinetics differ with the structure and geometry of the OC. They used the changing grain size model for reaction kinetics and chose a small particle size (between 30 and 70 μm) to minimize mass transfer effects. Hossain et al. [18] showed that the SCM with the surface chemical reaction being rate controlling well fits experimental data. This is because the OC particles used in CLC have a small diameter and a high internal porosity [51].

For the SCM with the reaction rate limiting over the volume of the particle is given by Eqs. 11, 12, and 13 [53, 56–58]. These are a rearranged version of the traditional SCM equation to allow the rate equation to be more easily entered into process simulators in the power law kinetics form.

$$-r_A = \frac{dC_A}{dt} = kC_A C_B^{2/3} \left[\frac{\text{kmol}}{\text{m}^3 \text{s}} \right] \quad (11)$$

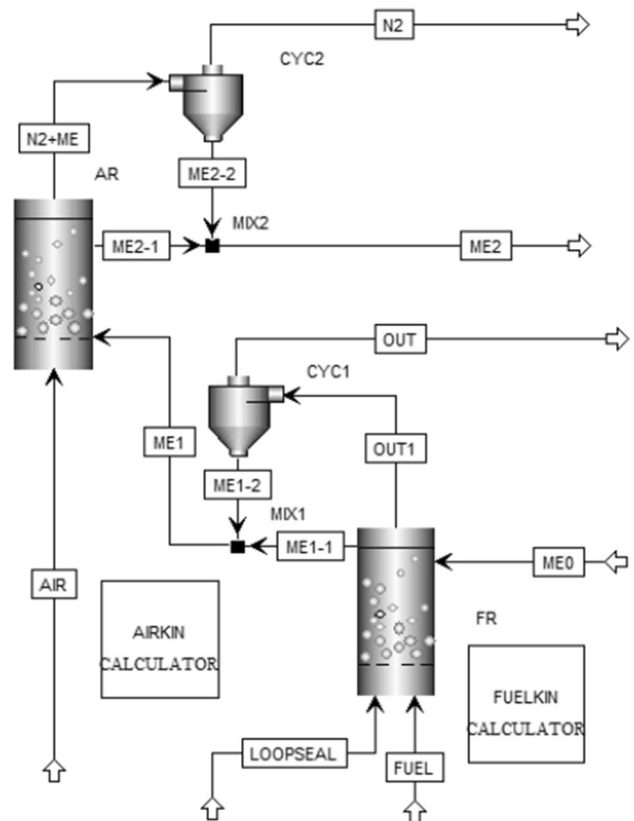
$$k = k_0 \exp\left(-\frac{E_A}{RT}\right) \left[\frac{1}{\text{s}} \left(\frac{\text{m}^3}{\text{kmol}} \right)^{2/3} \right] \quad (12)$$

$$k_0 = \frac{6}{d_p} \frac{k_{s0}}{C_{B0}^{2/3}} \left[\frac{1}{\text{s}} \left(\frac{\text{m}^3}{\text{kmol}} \right)^{2/3} \right] \quad (13)$$

where C_A is the bulk gas concentration of gas A, C_B is the current concentration of solid B [kmol/m³], C_{B0} is the initial concentration of solid B, k_{s0} is the rate constant for the first-order surface reaction [m/s], -r_A is the overall reaction rate of gas A normalized to the volume of the spherical particle of solid B [56], and d_p represents the outer diameter of the particle.

In process simulators, like Aspen Plus, it is usually more appropriate to give the concentrations in terms of the bulk volume and therefore Eq. 11 is used instead of a conversion based form. Converting the rate equation from the conversion based form to the concentration form was for convenience. Aspen Plus does not have a built in way to handle conversion based equations or the SCM. If the conversion based equation is desired it would have to be compiled using an external Fortran compiler, like Compaq Visual Fortran or Intel Visual Fortran. With the concentration based Arrhenius form, the reaction rate can be entered into Aspen Plus without external Fortran compilation. Only the initial concentration of the solid C_{B0} must be included into the pre-exponential factor by use of a calculator object in Aspen Plus.

Fig. 2 Aspen Plus dual fluidized bed CLC model



3 Aspen Plus implementation

The Chemical Looping Combustion (CLC) system in Aspen Plus consists of two Fluidized Bed (FB) reactors connected by a stream carrying the reduced Ni oxygen carrier (OC) from the fuel reactor (FR) to the air reactor (AR). The OC is oxidized in the AR and sent back to the FR. In the Aspen Plus simulation model (shown in Fig. 2) the OC is sent through the CLC system in a once through simulation, however, the OC is assumed to be recycled back from stream ME2 to ME0. The methane or syngas fuel is sent into the FR through the FUEL stream. The fuel is combusted in the FR and the exhaust exits the top of the reactor in the OUT1 stream where the solids are separated out by a cyclone and the remaining exhaust leaves the system in the OUT stream. The solids that exited the top of the FR (ME1-2) are joined with the solids exiting the normal solid outlet (ME1-1) into one stream entering the AR (ME1). Air enters the AR in the Air stream and oxidizes the OC. There is no usual solid outlet, but the Aspen Plus FB reactor requires one, so this stream (ME2-1) is assumed to exit at the top of the AR and joins the solids that are separated from the AR riser in the cyclone (ME2-2) into a single stream (ME2). The spent air with reduced oxygen content exits the AR at the top (N2 + ME) where the spent air (N2) is separated from the solids (ME2-2). Each cyclone is assumed to be 100% efficient at separating the solids from the gas.

3.1 Components

The IDEAL property method is used and Aspen Plus is set to estimate all missing parameters. Table 3 gives the components used in the Aspen Plus simulations.

3.2 Streams

The FUEL stream enters the FR at Normal Temperature and Pressure (NTP), that is 1 atm and 0 °C [38, 43]. The fuel gas flowrate entering the FR (Q_{FR}) was fixed at 170 L_N/h in all experiments. Using the Ideal Gas Law gives a molar density ρ_N ($\rho_N = n/V$) of 0.044615 mol/L corresponding to the molar volume V_N ($V_N = V/n$) of 22.414 L/mol, therefore, the molar flowrate of fuel is 7.5846 mol/h.

Table 3 Components used in the Aspen Plus model

Name	Type	Component name	Formula(s)	Databank
H2	Conventional	Hydrogen	H ₂	APV90.PURE35
H2O	Conventional	Water	H ₂ O	APV90.PURE35
CO	Conventional	Carbon-monoxide	CO	APV90.PURE35
CO2	Conventional	Carbon-dioxide	CO ₂	APV90.PURE35
CH4	Conventional	Methane	CH ₄	APV90.PURE35
O2	Conventional	Oxygen	O ₂	APV90.PURE35
N2	Conventional	Nitrogen	N ₂	APV90.PURE35
NI	Solid	Nickel	Ni	APV90.INORGANIC
NIO	Solid	Nickel-oxide	NiO	APV90.INORGANIC
NIO-D*	Solid	Nickel-oxide	NiO	APV90.INORGANIC
AL2O3	Solid	Aluminum-oxide-alpha, Corundum, Alumina	α-Al ₂ O ₃	APV90.PURE35

*NiO-D represents deactivated NiO and does not react. It also represents the NiO portion of NiAl₂O₄ which is not as reactive as NiO. Approximately 65% of the NiO in the particle is free when made and 35% considered deactivated. Up to 80% of the free NiO can be converted to NiAl₂O₄ [37, 55]. NiAl₂O₄ which is reactive but not as reactive as NiO, was not directly modeled in this research, so the percentage of "deactivated" NiO was varied

Table 4 Molar composition in percent volume of inlet gas streams

	Fuel stream during Syngas simulation (%)	Fuel stream during methane simulation	Air fuel stream
H ₂	25		
H ₂ O	0		
CO	15		
CO ₂	9		
CH ₄	0	30%	
O ₂	0		21%
N ₂	51	70%	79%

For some of the syngas experiments the gas feed was 15% CO, 9% CO₂, 25% H₂, and 51% N₂. For the methane experiments the methane was set at 30% and the remaining 70% was N₂. The molar composition is shown in Table 4.

The ME0 stream feeds the solid OC into the FR. The mass flowrate of solid NiO/α-Al₂O₃ cycling between the FR and the AR was 3 kg/h. The OC is initially 18% Ni and 82% Al₂O₃. However, only 65% of the Ni in the particle is free NiO. This percentage decreases with time because some of the free NiO converts to NiAl₂O₄ [37, 38, 55]. It was found that 75% of the Ni converts to free NiO each cycle so the free NiO can be as low as 20% with the rest being NiAl₂O₄ [38]. So, the percentage of free NiO was varied from 20 to 100% match the experimental data. It was found that a free NiO percentage of 50% fit the syngas data better, and a free NiO percent of 100% fit the methane better. This could be because the NiAl₂O₄, which is not directly modeled in this research, has a higher reactivity with methane as found in the literature [55]. A particle range is given in the studies as between 100 and 300 μm [37, 38], and so the particle size distribution (PSD) is assumed to be a normal distribution with a mean of $d_{p,D50} = 2e-4$ m and a standard deviation of $d_{p,STD} = 3.33e-5$ corresponding to the range divided by 6 to encompass three standard deviations from the mean ($P(\mu-3\sigma < x < \mu + 3\sigma) = 99.73\%$).

The AIR stream enters the AR at NTP (1 atm, 0 °C) [38, 43]. The air flowrate entering bottom of the AR as fluidizing gas was 720 LN/h. There is also a secondary air flow at the bottom of the riser above the bed of the AR (150 LN/h). The combined airflow into the AR is 870 LN/h. Again, using the Ideal Gas Law and a molar volume V_N of 22.414 L/mol, the molar flowrate of fuel is 38.815 mol/h. The AIR stream is considered 21% O₂ and 79% N₂.

The LOOPSEAL stream is pure N₂ and, since physically the loop seal gas mostly travels up into the FR, the LOOPSEAL stream is simulated as directly entering the FR. This LOOPSEAL stream is 37.5 LN/h and 100% N₂. In the simulation, it is considered as entering the FR directly. 37.5 LN/h corresponds to 1.673 mol/h using the Ideal Gas Law.

Table 5 Height and width of the air reactor (AR) [37, 38]

Location	Height (m)	Height (%)	Width (m)
Bottom of AR	0	0.00%	0.1
Top of AR Bed	0.1	8.47%	0.1
Top of AR Mixing Chamber	0.13	11.02%	0.1
Bottom of AR Riser	0.16	13.56%	0.02
Top of AR Riser	1.16	98.31%	0.02
Top of AR L-shape Exit	1.18	100.00%	0.02

3.3 Blocks

The Fuel Reactor (FR) is a bubbling bed and is simulated with the Aspen Plus V9.0 built-in Fluidized Bed (FB) unit processing the Solids Package. This FB unit process has many more options to configure and many that are required and not given an assumed or default value for example the orifices in the distributor. This specification is not usually given in literature. However, a figure from Kunii and Levenspiel [28, 44] was used to estimate the number of orifices per surface area from the common metric of $0.5 \text{ cm}^2/\text{orifice}$ ($A/n = 5e-5 \text{ m}^2/\text{orifice}$ or $n/A = 2 \text{ orifices/cm}^2$). Another complication of the FB unit process is that it requires the solid stream to have a particle size distribution (PSD). Most literature will give an average particle size, but usually not a range or distribution and so one must be assumed.

The FR has a total height (H_{FR}) of 0.4 m and a packed bed height (L_{FR}) of 0.1 m. The solid discharge location is assumed to be directly above the bed height at 25% of the height of the FR. The cross section is circular with a constant diameter (d_{FR}) of 0.05 m and total surface area (A_{FR}) of 0.002 m^2 . This surface area would correspond to an assumed 40 orifices on the perforated plate distributor. The orifice diameter was also assumed to be half of the side length of the A/n ratio ($d_o = \sqrt{(A/n)/2} = 0.003536 \text{ m}$). And the orifice discharge coefficient was left at the default value of 0.8. The FR operated at $T_{FR} = 1153 \text{ K}$. Both liquid and vapor phases were considered. The packed bed volume corresponded to an assumed bed mass of $W_{FR} = 0.485 \text{ kg}$. The particles were modeled as Geldart B type particles corresponding to sand type particles [59].

The CH_4 , CO , and H_2 oxidation reactions and the Water Gas Shift (WGS) reaction are specified to take place in the FR. Finally, options to help the simulation converge 10 cells were specified in the bottom zone and 10 in the top zone. The Newton solver was used for mass balance with a maximum of 100 iterations and an error tolerance of 0.001. The FR reactor was set to initialize using integration.

The Air Reactor (AR) is a fluidized bed in the fast fluidization regime. All of the bed mass is elutriated and travel up the riser and out of the top of the AR. The AR is simulated with the FB unit process.

The AR including the riser has a total height (H_{AR}) of 1.18 m and a packed bed height (L_{FR}) of 0.1 m. The mixing chamber is 0.13 m height where the diameter tapers in a cone shape to the more narrow riser section. The cone is 0.03 m tall. The riser is 1 m tall with an additional 0.02 m for the L shape of the pipe. The riser is 0.02 m in diameter (d_R) is 0.02 m. Table 5 shows the width along the height of the reactor as it is entered in Aspen Plus. The solid discharge location is assumed to be at the top of the riser, 100% of the AR height. The AR has an assumed 40 orifices on the perforated plate distributor. Again, the orifice diameter (d_o) is assumed to be 0.003536 m . And the orifice discharge coefficient was left at the default value of 0.8. The AR operates at $T_{AR} = 950 \text{ }^\circ\text{C}$. Both liquid and vapor phases were considered. The packed bed volume corresponded to an assumed initial bed mass of $W_{FR} = 0.485 \text{ kg}$, however, the FB cannot maintain this bed mass and all of the bed mass is elutriated. Again, the particles are Geldart B type particles. The Ni oxidation reaction is specified to take place in the AR. The same convergence options as the FR were used in the AR.

The mixers MIX1 and MIX2 were both set with default values corresponding to 0 pressure drop. Though the cyclones CYC1 and CYC2 were assumed 100% efficient at separating the gas from the solids, in reality this would take at least three cyclones in series to attain 99.98% efficiency (0.02% solids lost in exiting gas).

3.4 Reactions

See Table 6.

Table 6 Reaction kinetics used in simulation model

No.	Reaction	Kinetic expression (kmol/m ³ /s)	k ₀	E _a /ΔG° (kJ/kmol)	Source
1	CH ₄ + 4 NiO → CO ₂ + 2 H ₂ O + 4 Ni	$r_1 = \frac{6}{d_p} 0.0327 \exp\left(-\frac{37046}{RT}\right) C_{CH_4}^{-0.8} \left(\frac{C_{NiO}}{C_{NiO,0}}\right)^{2/3}$	0.0327 [m/s]	37,045.554	Ryu 2001 [45]
1K	CH ₄ + 4 NiO ↔ CO ₂ + 2 H ₂ O + 4 Ni	$K_{P1} = 1.9e19 \exp\left(-\frac{154907}{RT}\right)$ $T_{Kp=1} = 146.70^\circ\text{C}$	1.9e+19	154,906.52	Gibbs*
1r	CO ₂ + 2 H ₂ O + 4 Ni → CH ₄ + 4 NiO	$r_{1r} = \frac{6}{d_p} 1.21e-19 T^2 \exp\left(-\frac{117861}{RT}\right) \frac{C_{CO_2} C_{H_2O}^2}{C_{CH_4}} \left(\frac{C_{NiO}}{C_{NiO,0}}\right)^{2/3}$	$1.21e-19 \left[\frac{m^3}{s} \left(\frac{kmol}{kmol}\right)^2\right]$	-117,860.97	Calculated
2*	H ₂ + NiO → H ₂ O	$r_2 = \frac{6}{d_p} 9.3e-3 \exp\left(-\frac{26000}{RT}\right) C_{H_2}^{0.9} \left(\frac{C_{NiO}}{C_{NiO,0}}\right)^{2/3}$	9.3e-3 [m/s]	26,000	Abad 2007 [15]
3*	CO + NiO → CO ₂	$r_3 = \frac{6}{d_p} 5.2e-3 \exp\left(-\frac{25000}{RT}\right) C_{CO}^{0.9} \left(\frac{C_{NiO}}{C_{NiO,0}}\right)^{2/3}$	5.2e-3 [m/s]	25,000	Abad 2007 [15]
4	2 Ni + O ₂ → 2 NiO	$r_4 = \frac{6}{d_p} 1.8e-3 \exp\left(-\frac{7000}{RT}\right) C_{O_2} \left(\frac{C_{Ni}}{C_{Ni,0}}\right)^{2/3}$	1.8e-3 [m/s]	7000	Abad 2007 [15]
5	CH ₄ + NiO → CO + 2 H ₂ + Ni	$r_5 = \frac{6}{d_p} 1.31e8 \exp\left(-\frac{257526}{RT}\right) C_{CH_4}^{0.8} \left(\frac{C_{NiO}}{C_{NiO,0}}\right)^{2/3}$	1.31e+8 [m/s]	257,526	Rashidi 2013 [60] Dueso 2012 [55]
5K	CH ₄ + NiO ↔ CO + 2 H ₂ + Ni	$K_{P5} = 1.02e15 \exp\left(-\frac{215574}{RT}\right)$ $T_{Kp=1} = 477.01^\circ\text{C}$	1.02e+15	215,574.01	Gibbs*
5r	CO + 2 H ₂ + Ni → CH ₄ + NiO	$r_1 = \frac{6}{d_p} 8.84e-6 T^2 \exp\left(-\frac{41952}{RT}\right) \frac{C_{CO} C_{H_2}^2}{C_{CH_4}} \left(\frac{C_{NiO}}{C_{NiO,0}}\right)^{2/3}$	$8.84e-6 \left[\frac{m^3}{s} \left(\frac{kmol}{kmol}\right)^2\right]$	41,951.988	Calculated
6*	H ₂ O + CO ^c → H ₂ + CO ₂	$r_6 = 2777.78 \exp\left(-\frac{12560}{RT}\right) C_{CO} C_{H_2O}$	2777.78 [m ³ /kmol/s]	12,560	Biba 1978 [61] Gerber 2010 [62]
6K	H ₂ O + CO ↔ H ₂ + CO ₂	$K_{P6} = 0.01702 \exp\left(\frac{37238}{RT}\right)$ $T_{Kp=1} = 826.385^\circ\text{C}$	0.01702	-37,238.044	Gibbs*
6r	H ₂ + CO ₂ ^c → H ₂ O + CO	$r_{6r} = 163192 \exp\left(-\frac{49798}{RT}\right) C_{CO_2} C_{H_2}$	163,192 [m ³ /kmol/s]	49,798.044	Calculated
7	CH ₄ + H ₂ O ^{Ni} → CO + 3 H ₂	$r_7 = 0.71313 T \exp\left(-\frac{74720}{RT}\right) C_{CH_4} C_{H_2O}^{0.03}$	0.71313 [1/s/K]	74,720	Garcia-Vargus 2005 [63] Pham Minh 2018 [64]
7K	CH ₄ + H ₂ O ^{Ni} ↔ CO + 3 H ₂	$K_{P7} = 7.96e12 \exp\left(-\frac{220347}{RT}\right)$ $T_{Kp=1} = 619.013^\circ\text{C}$	7.96e+12	220,346.92	Wei 2004 [65] Gibbs*
7r	CO + 3 H ₂ ^{Ni} → CH ₄ + H ₂ O	$r_{7r} = 6.20e-12 T^3 \exp\left(\frac{145627}{RT}\right) C_{CO} C_{H_2}^3 C_{H_2O}^{-0.97}$	6.20e-12 [m ³ /kmol/s]	-145,626.92	Calculated
8	CH ₄ + CO ₂ ^{Ni} → 2 CO + 2 H ₂	$r_8 = 0.59024 T \exp\left(-\frac{70990}{RT}\right) C_{CH_4} C_{CO_2}^{0.03}$	0.59024 [m ³ /kmol/s]	70,990	Garcia-Vargus 2005 [63] Pham Minh 2018 [64] Wei 2004 [65]

Table 6 (continued)

No.	Reaction	Kinetic expression (kmol/m ³ /s)	k ₀	E _a /ΔG° (kJ/kmol)	Source
8K	CH ₄ + CO ₂ ^{Ni} ↔ 2 CO + 2 H ₂	$K_{p8} = 4.72e14 \exp\left(-\frac{257162}{RT}\right)$ $T_{Kp=1} = 642.233^\circ\text{C}$	4.72e+14	257,162.36	Gibbs*
8r	2 CO + 2 H ₂ ^{Ni} → CH ₄ + CO ₂	$r_{8r} = 8.64e-14 T^3 \exp\left(\frac{186172}{RT}\right) C_{CO}^2 C_{H_2}^{0.97} C_{CO_2}$	8.64e-14 [m ³ /kmol/s]	-186,172.36	Calculated
9	CH ₄ ^C → C + 2 H ₂	$r_9 = 5.4e3 \exp\left(-\frac{130959.2}{RT}\right) C_{CH_4}$	5.4e+3 [1/s]	130,959.2	Kobayashi 1992 [66]
9K	CH ₄ ↔ C + 2 H ₂	$K_{p5} = 403898 \exp\left(-\frac{87748}{RT}\right)$ $T_{Kp=1} = 544.401^\circ\text{C}$	403,898	87,748.323	Gibbs*
9r	C + 2 H ₂ ^C → CH ₄	$r_{9r} = 1.11e-1 T \exp\left(-\frac{43211}{RT}\right) C_{H_2}^{0.03} C_{CH_4}$	1.11e-1 [m ³ /kmol/s]	43,210.88	Calculated
10	C + H ₂ O ^C → CO + H ₂	$r_{10} = 3.6e12 \exp\left(-\frac{310000}{RT}\right) C_C C_{H_2O}$	3.6e+12 [m ³ /kmol/s]	310,000	Jess 1995 [67] Hobbs 1992 [68]
11	C + CO ₂ ^C → 2 CO	$r_{11} = 3.6e12 \exp\left(-\frac{310000}{RT}\right) C_C C_{CO_2}$	3.6e+12 [m ³ /kmol/s]	310,000	Jess 1995 [67] Hobbs 1992 [68]

(*):

The reaction order of the H₂ and CO combustion reactions has been adjusted from the literature sources. All Equilibrium expressions were simulated in Aspen using an RGibbs reactor and fitted using an Arrhenius plot. Equations were checked against literature where available. See discussion in the appendix.

Equilibrium Constants are given as Partial Pressure based K_p. The formula is converted back to concentration based K_c when determining the reverse reaction rate equation. K_p = K_c(RT)^{Δn}. The Water Gas Shift reaction rate equation given by Biba 1978 is catalyzed by char. This reaction rate was assumed to be the same for nickel. Actually, the literature [63, 64] shows that when catalyzed by nickel the reaction may be as much as 50 times fast, but there is much variation in water gas shift reaction rate data in general.

The more commonly used kinetic rate equation for the WGS and SMR reactions over nickel published by Xu and Ferment [69] is of Langmuir–Hinshelwood–Hougen–Watson (LHHW) form and was not as easily simplified to a power law form. It was desired for this kinetic model to contain all power law rate equations for simplicity.

Wei et al. 2004 show that methane reforming is essentially a decomposition reaction with a char gasification reaction, and that breaking the C–H bond in the methane is almost totally independent of the agent used for reforming (CO₂ or H₂O).

An exponent of very small magnitude (n = 0.03) is added to reactions 7, 8 and 9r to make numerical solving easier when the component concentration nears zero. The original versions of the reaction rate equation did not have the 0.03 exponent.

Only reaction 4 occurs in the AR. In the syngas combustion simulation, only reactions 2, 3, 6 and 6r occur in the FR. In the methane combustion simulation, all reactions listed are considered.

Fig. 3 FR Outlet H_2 mole fraction vs. OC mass flowrate F_s (kg/h) for $T_{FR}=880$ °C with standard error bars comparing FB simulation to Gibbs equilibrium model [37]

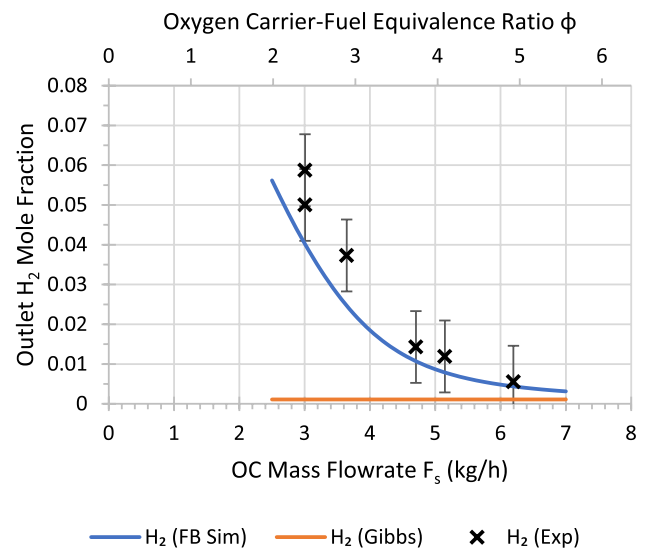
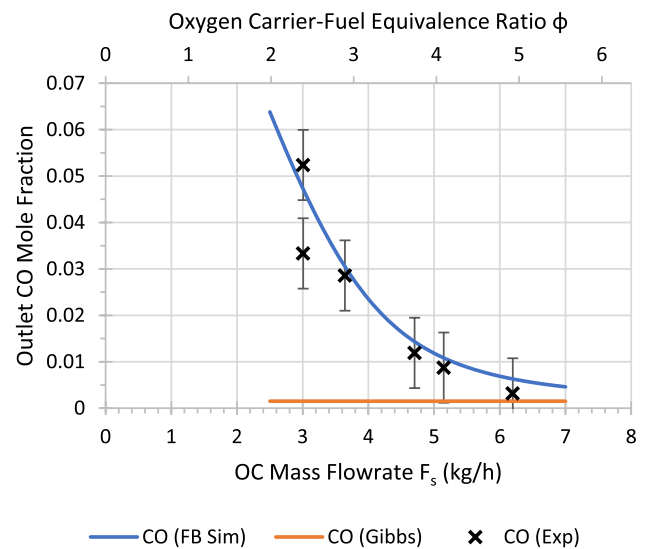


Fig. 4 FR Outlet CO mole fraction vs. OC mass flowrate F_s (kg/h) for $T_{FR}=880$ °C with standard error bars comparing FB simulation to Gibbs equilibrium model [37]



4 Results and discussion

4.1 Syngas chemical looping combustion experiments

The Aspen Plus simulation well fit the data using the kinetics described in Table 6 [37]. As the amount of oxygen entering the system increases the mole fraction of H_2 and CO decrease and the combustion efficiency increases. Figures 3 and 4 show the mole fraction of H_2 and CO respectively versus the oxygen carrier mass flowrate for the FB-unit kinetic model compared against RGibbs equilibrium model and experimental data. As more oxygen is available for combustion (a higher OC mass flowrate) less H_2 and CO is in the outlet gas from the fuel reactor. The simulation results were within two percentage points of the outlet gas molar composition for both H_2 and CO.

Figure 5 shows the affect of the molar air flowrate on the conversion of Ni and O_2 . The conversion of Ni to NiO quickly plateaus at almost full conversion after around 6 mol/h. After this point, more air is supplied than needed, and there is excess oxygen so the conversion of oxygen goes down.

Figure 6 shows the molar composition of the FR outlet gas versus the molar flow rate of the fuel entering the FR. The combustion of syngas peaks at about 5 mol/h. This is because after this point the metal oxide is saturated and

Fig. 5 Conversion of Ni (X_{Ni}) and O₂ (X_{O_2}) vs. air molar flowrate (N_{AR}) [mol/h]

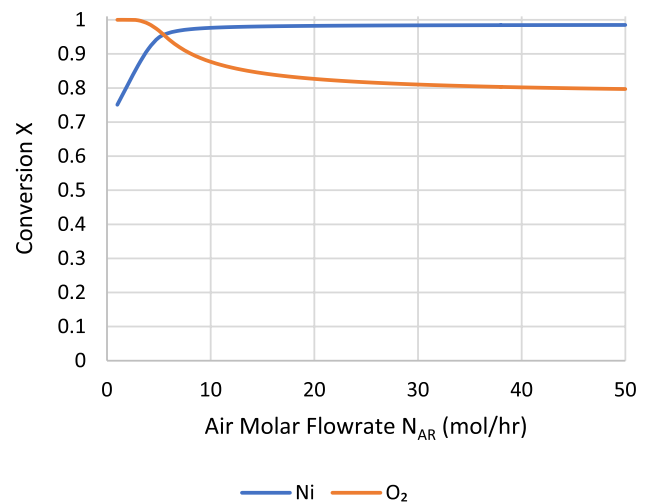


Fig. 6 Molar Composition of Outlet Gas vs. fuel molar flowrate (N_{FR}) [mol/h]

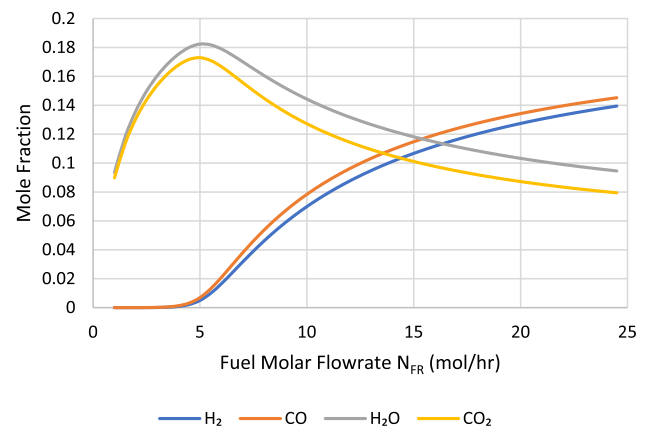
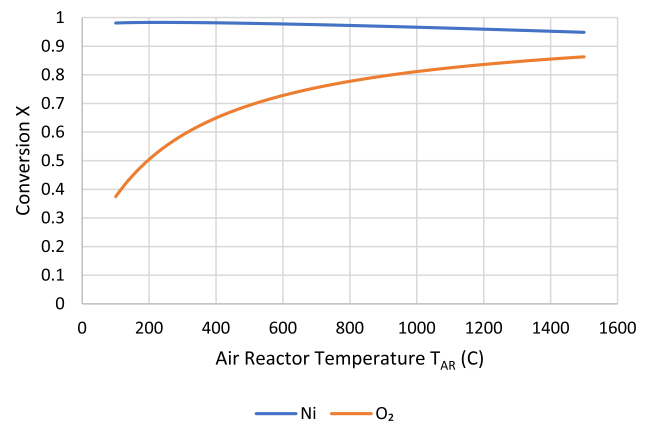


Fig. 7 Conversion of Ni (X_{Ni}) and O₂ (X_{O_2}) vs. air reactor temperature (T_{AR}) [C]



there is not more oxygen to convert the increased amount of fuel. This then dilutes the combusted products in the unreacted fuel exiting the reactor.

Increasing the temperature increases the conversion rate of oxygen. This is seen by the increasing conversion of O₂ in Fig. 7. However, the conversion was calculated for both the O₂ gas and the solid Ni as molar concentrations. This means that as the temperature increases the volume of gas increases and the concentration of converted solid decreases slightly.

Increasing the temperature of the FR T_{FR} increases the combustion rate for CO and H₂. The increased temperature also increases the rate of the water–gas shift (WGS) reaction. At temperatures above around 826 °C the WGS reaction works in reverse to convert H₂ and CO₂ into CO and H₂O. These two dynamics can be seen in Fig. 8.

Fig. 8 Molar Composition of Outlet Gas vs. fuel reactor temperature (T_{FR}) [°C]

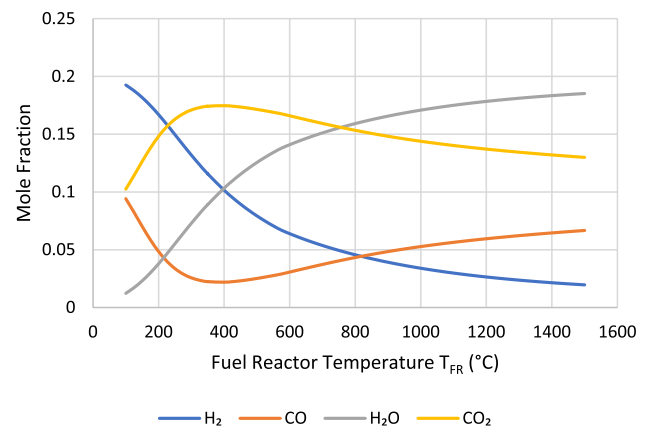
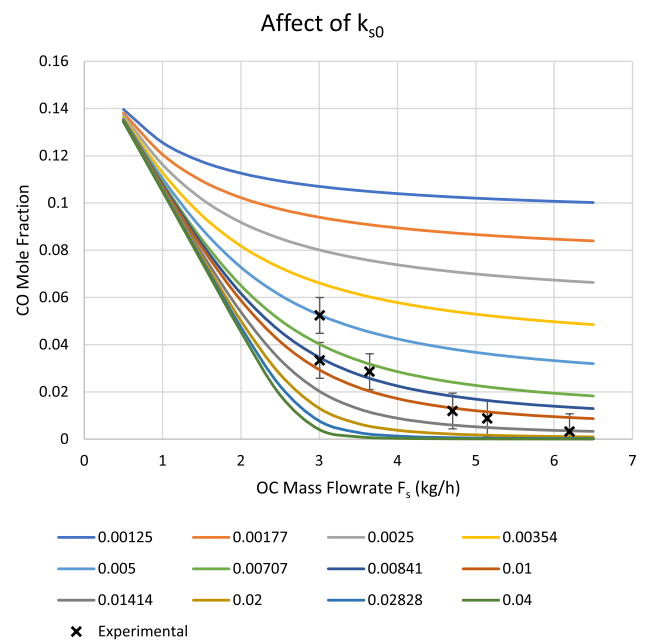


Fig. 9 CO mole fraction vs. OC mass flowrate for different k_{s0} values



4.2 Sensitivity analysis

In Fig. 9, the plot of the CO mole fraction versus OC Mass Flowrate was shown for different pre-exponential factors k_{s0} for Reaction 3 in Table 6. It shows what would be expected that the combustion reaction rate increases as k_{s0} increases and therefore the mole fraction of CO decreases.

Figure 10 shows how the mole fraction versus OC mass flowrate differs for different exponents of the gas concentration in the CO combustion reaction rate equation (Reaction 3). Smaller exponents make the reaction rate less dependent on the gas concentration and therefore faster. With a faster reaction rate there is less product gas at the same OC flowrate.

In the three dimensional (3D) Shrinking Core Method (SCM), the order of the solid conversion factor is $2/3 (1-X_B)^{2/3}$. However, in the one-dimensional (1D) SCM the exponent of the solid conversion is 2 (i.e., $(1-X_B)^2$). Figure 11 shows the effect of varying the exponent of the solid conversion in the SCM for Reaction 3. The value of $m = 2/3$ would be the 3D SCM and a value of $m = 2$ would be the equivalent of the 1D SCM. It is shown that the 3D SCM best fits the data with a value of $m = 0.667$.

The percentage of free NiO is around 50% (between 20 and 65%) [70]. Dueso et al. [37, 55] note that the fresh OC particles have approximately 65% of the NiO free. Furthermore, over continuous operation of the CLC system, over 25% of the free NiO is converted to $NiAl_2O_4$ which does act as an oxygen carrier but has a much lower reactivity than NiO. Therefore, for this simulation the inactive NiO is considered at 51.25%, including the initially inactive NiO and the NiO

Fig. 10 CO mole fraction vs. OC mass flowrate F_s for different gas reaction orders n

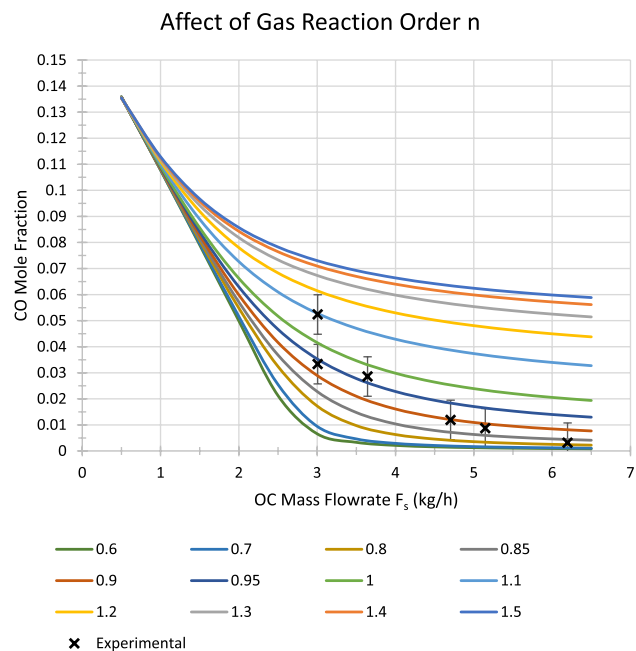
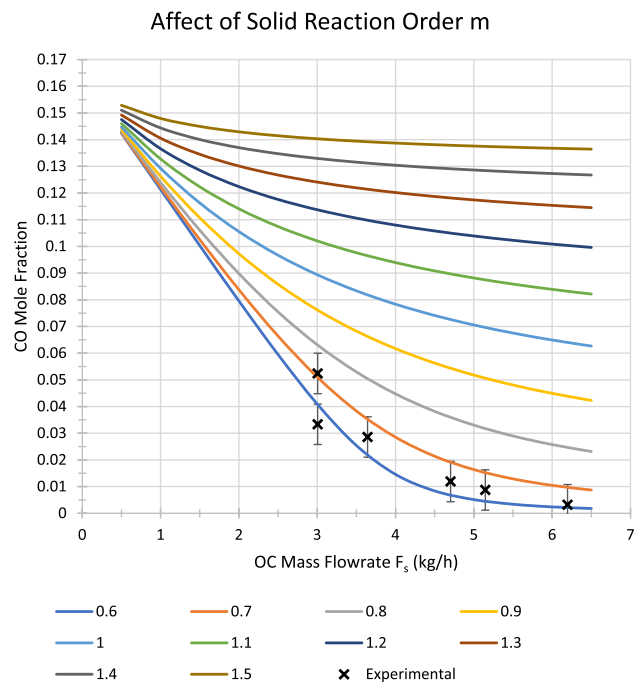


Fig. 11 CO mole fraction vs. OC mass flowrate F_s for different solid reaction orders m



portion of $NiAl_2O_4$. Figure 12 shows the effect of considering different percentages of inactive NiO. Considering higher portions of inactive NiO essentially stretches the graph horizontally, because more OC is required to have the same amount of available oxygen.

A similar analysis was performed for H_2 in Reaction 2. These plots confirm the parameters of the SCM and the kinetic rate equation shown in Table 6.

4.3 Methane experiments

Figure 13 shows the mole fraction of the FR outlet gas versus the OC mass flowrate for the kinetic simulation compared to experimental data. The methane combustion simulation assumes no inactive NiO. The conversion of NiO to $NiAl_2O_4$

Fig. 12 CO mole fraction vs. OC mass flowrate F_s for different values of inactive NiO $w_{\text{NiO-D}}$

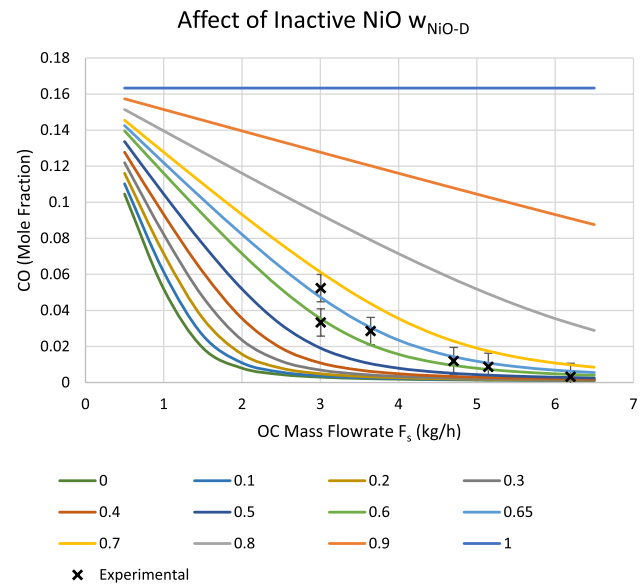
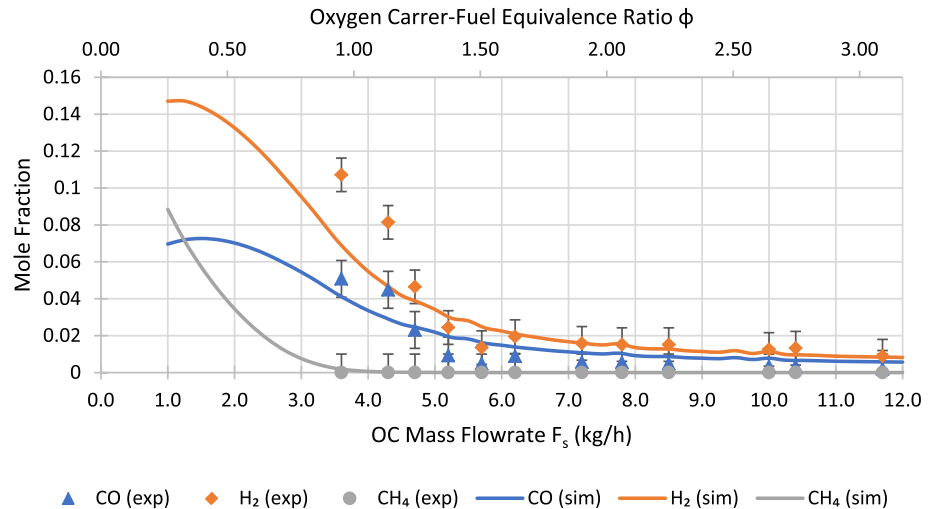


Fig. 13 Solid OC mass flowrate F_s (kg/h) vs. outlet gas composition (mole fraction) with 1% error bars for methane combustion experiment assuming all free NiO. $T_{\text{FR}} = 880$ °C, methane flow = 50 L_{N}/h



did not seem to affect the methane experiment. This may indicate that CH_4 has a higher reactivity to NiAl_2O_4 than the H_2 and CO in syngas. This seems to agree with more recent work from Dueso et al. [55]. However, because the species NiAl_2O_4 was not considered with separate reactivities, all of the Ni was modeled as free NiO for the methane experiment. For the methane experiments, the simulation results were within four percentage points of the outlet gas molar composition for H_2 , within two percentage points for CO , and less than one percentage point for methane.

5 Conclusions

In this research, a circulating chemical looping combustion (CLC) process is simulated and analyzed. The CLC system is composed of a fuel reactor which is a fluidized bed operating as a bubbling bed flow regime and an air reactor operating in fast fluidization flow regime. The reactions occurring in each reactor are non-catalytic heterogeneous gas–solid reactions. The shrinking core model (SCM) was used to describe the kinetics. The build-in Fluidized Bed unit process was used in Aspen Plus to simulate the complex hydrodynamics of the fluidized bed for the fuel and the air reactors. Syngas and methane are considered as the gas inflow to the fuel reactor and pure air is the gas inflow to the air reactor. Cycling between the two reactors is the nickel oxide (NiO/Ni) oxygen carrier (OC) supported by bentonite

which transfers oxygen between the fuel and air reactors undergoing reduction and oxidation (redox) reactions in each reactor respectively. The entire CLC process is modeled in Aspen Plus and various operating parameters were explored.

The results show that:

- The built-in FB unit process accounts for the hydrodynamic and kinetic processes, and its complexity is a midway between low resolution models (e.g., single PFR or CSTR models, the two-phase model) and more complex models like computational fluid dynamics (CFD) models.
- This model and the FB unit account for reactor geometry (i.e., diameter, height, etc.), solid inventory, and the air–fuel ratio.
- Comparing this FB unit process model with other model types, such as the Gibbs equilibrium model, the FB unit gives a more accurate and realistic prediction of the outlet syngas, within 2% of the experimental data for syngas combustion and within 4% for methane combustion.
- This model makes it possible to size the FB reactors and therefore get an estimate of the thermal and economic efficiency.
- Because this model converts all core-shrinking kinetics into power law forms, it can be run in Aspen Plus without the need for external Fortran compilation. This is a major advantage of this kinetic model over other external Fortran based models, such as those discussed in the introduction [21, 33–35, 71].

6 Future work

Many improvements can be made to this work. It is the hope of the authors that the model and data files will be useful for any other researchers attempting to replicate or improve upon this work. Examples of future improvements are:

- Comparing the Aspen Plus FB unit process to other types of kinetic models in Aspen Plus, such as a single PFR, single CSTR, CSTRs in series, or CSTR-PFR pairs in series with mass and energy exchange representing the two-phase model [21].
- Testing various parameters and assumptions of the FB unit process, such as the number of bed stages or the number of free board stages, etc.

Acknowledgements This project was fully (or partially) supported by funds provided by an NSF-CREST Project (Award Numbers: 1242152 and 2112679). Its contents are solely the responsibility of the authors and do not necessarily represent the official views of the funding agency.

Author contributions MJ: Writing—original draft preparation, conceptualization, methodology, investigation and analysis. AS: Supervision, writing—reviewing and editing, funding acquisition. KS: Supervision, writing—reviewing and editing, funding acquisition. FL: Supervision, writing—reviewing and editing. LW: Conceptualization, supervision, writing—reviewing and editing, funding acquisition. All authors read and approved the final manuscript.

Funding This project was fully (or partially) supported by funds provided by an NSF-CREST Project (Award Numbers: 1242152 and 2112679). Its contents are solely the responsibility of the authors and do not necessarily represent the official views of the funding agency.

Data availability All data and code are available at: <https://bit.ly/Jasper-2022-DCE>.

Code availability All data and code are available at: <https://bit.ly/Jasper-2022-DCE>.

Declarations

Please note that this research was part of a PhD dissertation entitled: Multi-Objective Optimization and Techno-Economic-Environmental Analysis of Biomass Gasification and Pathways for Transportation Fuel. Jasper, Micah Nathanael. North Carolina Agricultural and Technical State University ProQuest Dissertations Publishing, 2021. 28768239. <http://ncat.idm.oclc.org/login?url=https://www.proquest.com/dissertations-theses/multi-objective-optimization-techno-economic/docview/2631906103/se-2>.

Competing interests The authors declare that they have no known competing financial interests or personal relationships that could have appeared to influence the work reported in this paper.

Open Access This article is licensed under a Creative Commons Attribution 4.0 International License, which permits use, sharing, adaptation, distribution and reproduction in any medium or format, as long as you give appropriate credit to the original author(s) and the source, provide a link to the Creative Commons licence, and indicate if changes were made. The images or other third party material in this article are included in the article's Creative Commons licence, unless indicated otherwise in a credit line to the material. If material is not included in the article's Creative Commons licence and your intended use is not permitted by statutory regulation or exceeds the permitted use, you will need to obtain permission directly from the copyright holder. To view a copy of this licence, visit <http://creativecommons.org/licenses/by/4.0/>.

References

1. EPA, *Inventory of U.S. Greenhouse Gas Emissions and Sinks 1990–2019*. 2021, United States Environmental Protection Agency.
2. Bryant E. *Climate process and change*. 1st ed. Cambridge: Cambridge University Press; 1997.
3. Blockstein DE, Shockley MA. *Energy for a sustainable and secure future: a report of the sixth National Conference on Science, Policy and the Environment*: January 26–27, 2006. Washington: National Council for Science and the Environment; 2006.
4. Herzog HJ. The economics of CO₂ capture. In: Riemer P, Wokaun A, editors. *Proceedings of the fourth international conference of greenhouse gas control technologies*. London: Pergamon Press; 1999. p. 101–6.
5. Abu-Zahra MRM, et al. CO₂ capture from power plants: Part I. A parametric study of the technical performance based on monoethanolamine. *Int J Greenh Gas Control*. 2007;1(1):37–46.
6. Abu-Zahra MRM, et al. CO₂ capture from power plants: Part II. A parametric study of the economical performance based on monoethanolamine. *Int J Greenh Gas Control*. 2007;1(2):135–42.
7. Singh D, et al. Techno-economic study of CO₂ capture from an existing coal-fired power plant: MEA scrubbing vs. O₂/CO₂ recycle combustion. *Energy Convers Manage*. 2003;44(19):3073–91.
8. Richter HJ, Knoche KF. *Reversibility of Combustion Processes, in Efficiency and Costing*. 1983, American Chemical Society. p. 71–85.
9. Ishida M, Zheng D, Akehata T. Evaluation of a chemical-looping-combustion power-generation system by graphic exergy analysis. *Energy*. 1987;12(2):147–54.
10. Wolf J, Anhedén M, Yan J. Comparison of nickel- and iron-based oxygen carriers in chemical looping combustion for CO₂ capture in power generation. *Fuel*. 2005;84(7):993–1006.
11. Kerr HR. Chapter 38 - capture and separation technology gaps and priority research needs. In: Thomas DC, Benson S, editors. *Carbon dioxide capture for storage in deep geologic formations*. Amsterdam: Elsevier; 2005. p. 655–60.
12. Metz B, et al. *IPCC special report on carbon dioxide capture and storage*. Cambridge: Cambridge University Press; 2005.
13. Fleiß B, et al. Holistic assessment of oxygen carriers for chemical looping combustion based on laboratory experiments and validation in 80 kW pilot plant. *Fuel Process Technol*. 2022;231: 107249.
14. Mercado JP, et al. Life cycle assessment of a biomass based chemical looping combustion. *Environ Res*. 2023;217: 114876.
15. Abad A, et al. Mapping of the range of operational conditions for Cu-, Fe-, and Ni-based oxygen carriers in chemical-looping combustion. *Chem Eng Sci*. 2007;62(1):533–49.
16. García-Labiano F, et al. Effect of pressure on the behavior of Copper-, Iron-, and Nickel-based oxygen carriers for chemical-looping combustion. *Energy Fuels*. 2006;20(1):26–33.
17. Adáñez J, et al. Selection of oxygen carriers for chemical-looping combustion. *Energy Fuels*. 2004;18(2):371–7.
18. Hossain MM, de Lasa HI. Chemical-looping combustion (CLC) for inherent CO₂ separations—a review. *Chem Eng Sci*. 2008;63(18):4433–51.
19. Ishida M, Jin H. A novel chemical-looping combustor without NO_x formation. *Ind Eng Chem Res*. 1996;35(7):2469–72.
20. Heyes AL, et al., *A Thermodynamic analysis of chemical looping combustion*. 2011, p. 105–111.
21. Porrazzo R, White G, Ocone R. Aspen Plus simulations of fluidized beds for chemical looping combustion. *Fuel*. 2014;136:46–56.
22. Fan LS. *Chemical Looping Systems for Fossil Energy Conversions*. 2010.
23. Hatanaka T, Matsuda S, Hatanaka H. A new-concept gas-solid combustion system "MERIT" for high combustion efficiency and low emissions. In: *IECEC-97 Proceedings of the Thirty-Second Intersociety Energy Conversion Engineering Conference (Cat. No. 97CH6203)*. 1997.
24. Jafari R, Sotudeh-Gharebagh R, Mostoufi N. Modular simulation of fluidized bed reactors. *Chem Eng Technol*. 2004;27(2):123–9.
25. Li F, et al. Syngas chemical looping gasification process: oxygen carrier particle selection and performance. *Energy Fuels*. 2009;23(8):4182–9.
26. Cui H, Mostoufi N, Chaouki J. Gas and solids between dynamic bubble and emulsion in gas-fluidized beds. *Powder Technol*. 2001;120(1–2):12.
27. Cui HP, Mostoufi N, Chaouki J. Characterization of dynamic gas-solid distribution in fluidized beds. *Chem Eng J*. 2000;79(2):133–5.
28. Kunii D, Levenspiel O. *Fluidization Engineering (Second Edition)*. Fluidization Engineering (Second Edition), ed. D. Kunii and O. Levenspiel. 1991, Boston: Butterworth-Heinemann.
29. Sarvar-Amini A, et al. Sequential simulation of a fluidized bed membrane reactor for the steam methane reforming using ASPEN PLUS. *Energy Fuels*. 2007;21(6):3593–8.
30. Sotudeh-Gharebaagh R, et al. Simulation of circulating fluidized bed reactors using ASPEN PLUS. *Fuel*. 1998;77(4):327–37.
31. Liu B, et al. Process simulation of formation and emission of NO and N₂O during coal decoupling combustion in a circulating fluidized bed combustor using Aspen Plus. *Chem Eng Sci*. 2012;71:375–91.
32. Hashemi Sohi A, et al. Sequential-based process modeling of natural gas combustion in a fluidized bed reactor. *Energy Fuels*. 2012;26(4):2058–67.
33. Rafati M, et al. Sequential modular simulation of hydrodynamics and reaction kinetics in a biomass bubbling fluidized-bed gasifier using Aspen Plus. *Energy Fuels*. 2015;29(12):8261–72.
34. Ohlemuller P, et al. Development of a process model for coal chemical looping combustion and validation against 100 kW(th) tests. *Appl Energy*. 2015;157:433–48.
35. Ohlemuller P, et al. Development and validation of a 1D process model with autothermal operation of a 1 MW(th) chemical looping pilot plant. *Int J Greenh Gas Control*. 2018;73:29–41.

36. Puig-Gamero M, et al. Simulation of biomass gasification in bubbling fluidized bed reactor using aspen plus®. *Energy Convers Manage.* 2021;235: 113981.
37. Dueso C, et al. Syngas combustion in a chemical-looping combustion system using an impregnated Ni-based oxygen carrier. *Fuel.* 2009;88(12):2357–64.
38. Adánez J, et al. Methane combustion in a 500 Wth chemical-looping combustion system using an impregnated Ni-Based oxygen carrier. *Energy Fuels.* 2009;23(1):130–42.
39. Jasper MN. *Multi-Objective Optimization and Techno-Economic-Environmental Analysis of Biomass Gasification and Pathways for Transportation Fuel.* In *Energy & Environmental Systems.* 2021, North Carolina Agricultural and Technical State University: Greensboro, NC. p. 163.
40. de Diego LF, et al. Hydrogen production by chemical-looping reforming in a circulating fluidized bed reactor using Ni-based oxygen carriers. *J Power Sources.* 2009;192(1):27–34.
41. Davidson JF, Harrison D. *Fluidised particles.* New York: Cambridge University Press; 1963.
42. Davidson JF, Harrison D, Jackson R. Fluidized particles. In: Guazzelli E, Oger L, editors. *Mobile particulate systems.* Dordrecht: Springer; 1995.
43. Bronkhorst. *SCCM, l/min or other Mass Flow units, where do they stand for?* 2021; <https://www.massflow-online.com/faqs/what-do-lmin-lsmin-slm-and-sccm-stand-for/>. Accessed 7 Jan 2021.
44. Mori S, Wen CY. Estimation of bubble diameter in gaseous fluidized beds. *AIChE J.* 1975;21:109.
45. Ryu H-J, et al. Oxidation and reduction characteristics of oxygen carrier particles and reaction kinetics by unreacted core model. *Korean J Chem Eng.* 2001;18(6):831–7.
46. Mattison T, Järnäs A, Lyngfelt A. Reactivity of some metal oxides supported on alumina with alternating methane and oxygen-application for chemical-looping combustion. *Energy Fuels.* 2003;17:651.
47. Mattison T, Lyngfelt A, Cho P. The use of iron oxide as an oxygen carrier in chemical-looping combustion of methane with inherent separation of CO₂. *Fuel.* 2001;80(13):1953–62.
48. Son SR, Kim SD. Chemical-looping combustion with NiO and Fe₂O₃ in a thermobalance and circulating fluidized bed reactor with double loops. *Ind Eng Chem Res.* 2006;45(8):2689–96.
49. Lyngfelt A, Leckner B, Mattisson T. A fluidized-bed combustion process with inherent CO₂ separation; application of chemical-looping combustion. *Chem Eng Sci.* 2001;56(10):3101–13.
50. García-Labiano F, et al. Temperature variations in the oxygen carrier particles during their reduction and oxidation in a chemical-looping combustion system. *Chem Eng Sci.* 2005;60(3):851–62.
51. Abad A, et al. Modeling of the chemical-looping combustion of methane using a Cu-based oxygen-carrier. *Combust Flame.* 2010;157(3):602–15.
52. Abad A, et al. Fuel reactor model validation: assessment of the key parameters affecting the chemical-looping combustion of coal. *Int J Greenh Gas Control.* 2013;19:541–51.
53. Levenspiel O. *Chemical Reaction Engineering.* 3 ed. 1999.
54. Marbán G, García-Calzada M, Fuertes AB. Kinetics of oxidation of CaS particles in the regime of low SO₂ release. *Chem Eng Sci.* 1999;54(1):77–90.
55. Dueso C, et al. Reduction and oxidation kinetics of nickel-based oxygen-carriers for chemical-looping combustion and chemical-looping reforming. *Chem Eng J.* 2012;188:142–54.
56. Missen RW, Mims CA, Saville BA. *Introduction to chemical reaction engineering and kinetics.* New York: Wiley; 1999.
57. Fogler HS. *Elements of chemical reaction engineering,* 5th edition. 5th ed. Boston: Pearson Education Inc.; 2016.
58. Schmidt LD. *The engineering of chemical reactions.* New York: Oxford University Press; 1998.
59. Cocco R, Karri SR, Knowlton T. *Introduction to Fluidization.* *Chem Eng Prog.* 2014;110(11):21–9.
60. Rashidi H, Ebrahim HA, Dabir B. Reduction kinetics of nickel oxide by methane as reducing agent based on thermogravimetry. *Thermo-chim Acta.* 2013;561:41–8.
61. Biba V, et al. Mathematical model for the gasification of coal under pressure. *Ind Eng Chem Process Des Dev.* 1978;17(1):92–8.
62. Gerber S, Behrendt F, Oevermann M. An Eulerian modeling approach of wood gasification in a bubbling fluidized bed reactor using char as bed material. *Fuel.* 2010;89(10):2903–17.
63. García-Vargas JM, et al. Catalytic and kinetic analysis of the methane tri-reforming over a Ni–Mg/β-SiC catalyst. *Int J Hydrogen Energy.* 2015;40(28):8677–87.
64. Pham Minh D, et al. Chapter 4—hydrogen production from biogas reforming: an overview of steam reforming, dry reforming, dual reforming, and tri-reforming of methane. In: Azzaro-Pantel C, editor., et al., *Hydrogen supply chains.* Cambridge: Academic Press; 2018. p. 111–66.
65. Wei J, Iglesia E. Isotopic and kinetic assessment of the mechanism of reactions of CH₄ with CO₂ or H₂O to form synthesis gas and carbon on nickel catalysts. *J Catal.* 2004;224(2):370–83.
66. Kobayashi A, Steinberg M. *The thermal decomposition of methane in a tubular reactor.* 1992: United States.
67. Jess A. Mechanisms and kinetics of thermal reactions of aromatic hydrocarbons from pyrolysis of solid fuels. *Fuel.* 1996;75(12):1441–8.
68. Hobbs ML, Radulovic PT, Smoot LD. Modeling fixed-bed coal gasifiers. *AIChE J.* 1992;38(5):681–702.
69. Xu J, Froment GF. Methane steam reforming, methanation and water-gas shift: I. Intrinsic kinetics *AIChE Journal.* 1989;35(1):88–96.
70. Zafar Q, et al. Reaction kinetics of freeze-granulated NiO/MgAl₂O₄ oxygen carrier particles for chemical-looping combustion. *Energy Fuels.* 2007;21(2):610–8.
71. Rafati M, et al. Techno-economic analysis of production of Fischer-Tropsch liquids via biomass gasification: the effects of Fischer-Tropsch catalysts and natural gas co-feeding. *Energy Convers Manage.* 2017;133:153–66.